Orbital Angular Momentum Control of Entanglement in Dual-Cavity Ring Bose–Einstein Condensates

Muqaddar Abbas[1, 2, *] and Ghaisud Din[2, †]

[1] *Department of Basic Teaching and Research, Shenyang Urban Construction University, Shenyang, 110167, China*
[2] *Ministry of Education Key Laboratory for Nonequilibrium Synthesis and Modulation of Condensed Matter, Shaanxi Province Key Laboratory of Quantum Information and Quantum Optoelectronic Devices, School of Physics, Xi'an Jiaotong University, Xi'an 710049, China*

(Dated: January 7, 2026)

We study quantum correlations in a system of two optically coupled cavities, each containing a ring-shaped Bose–Einstein condensate confined in a toroidal potential. The condensates interact with cavity fields through an angular optical lattice generated by degenerate modes carrying opposite orbital angular momentum (OAM), while photon hopping mediates inter-cavity coupling. Using a linearized quantum Langevin formalism, we analyze the steady-state covariance matrix and quantify bipartite along with tripartite entanglement among collective atomic side modes and cavity fields. We show that OAM and photon hopping provide efficient control over the strength and distribution of quantum correlations, enabling entanglement between spatially separated condensates. The robustness of these correlations against thermal effects is examined, revealing enhanced stability of atom–cavity entanglement compared to purely atomic correlations. Phase-space representations based on Wigner functions are used to illustrate the steady-state fluctuation dynamics. Our results establish coupled cavity systems with ring-shaped condensates as a tunable platform for controlled matter–light correlations.

I. Introduction

Quantum entanglement [1] has become a cornerstone of modern quantum science and emerging quantum technologies [2]. While early experimental realizations focused on microscopic entities such as single particles and atoms [2, 3], it is now recognized that entanglement also manifests in mesoscopic and even macroscopic systems. Owing to its intrinsically nonclassical character, entanglement offers a powerful tool for exploring the fundamental structure of quantum theory and for experimentally examining foundational principles of physics [4].

Significant progress toward these goals has been made in the areas of cavity optomechanics and quantum information science [5]. An important early theoretical result was provided by Vitali *et al.*, who showed that the radiation field inside an optical cavity can become entangled with the vibrational motion of a macroscopic mechanical resonator [6]. Building on this work, subsequent investigations demonstrated the emergence of optomechanical entanglement, as well as the generation of squeezed mechanical states, underscoring the flexibility of optomechanical architectures [7]. As a result, extensive research has been devoted to understanding the creation, manipulation, and measurement of quantum correlations in optomechanical systems [8–14].

Beyond their importance for fundamental physics, optomechanical systems have attracted considerable interest due to their potential technological impact. Notable applications include the ultrasensitive detection of weak forces [15, 16], gravitational-wave observatories [17], the design of high-performance mechanical resonators [18], and detection protocols operating at the single-photon level [5, 19]. Owing to these capabilities, optomechanical platforms are regarded as strong contenders for next-generation quantum technologies.

Alongside these advances, Bose–Einstein condensates (BECs) realized in annular trapping configurations have emerged as a powerful platform for investigating coherent matter-wave behavior and quantum fluid dynamics [20–23]. In such closed geometries, the requirement that the condensate wavefunction be single valued imposes discrete phase winding numbers, which in turn lead to the formation of persistent superfluid flows [24]. These circulating currents can exhibit remarkable long-term stability [25–27], and under appropriate conditions they give rise to states with larger circulation that are protected by topology [28]. As a consequence of these features, ring-shaped BECs have been widely employed to explore superfluid hydrodynamics [29, 30], implement matter-wave interferometric schemes [31], develop atomtronic circuits [32, 33], and study fermionic superfluid phases [34–36].

One of the central experimental difficulties in these platforms is the precise measurement of the condensate's circulation. The rotational configuration is quantified by the integer phase winding number associated with the macroscopic wavefunction, and reliable access to this parameter is crucial for both fundamental investigations and practical implementations. Standard diagnostic techniques are based on absorption imaging, which is intrinsically destructive and therefore incompatible with continuous observation [20]. In addition, characteristic length scales of the system, including the vortex core and the radial thickness of the ring, are frequently below the optical wavelength, making direct detection challenging.

* muqaddarabbas@outlook.com
† dinghaisud@stu.xjtu.edu.cn

Consequently, circulation is most often inferred after a time of flight expansion that magnifies these features [37], at the cost of losing real-time monitoring and feedback.

To address these challenges, a recently proposed scheme [38] employs optomechanical interactions to detect and regulate the circulation of a ring-shaped BEC with minimal disturbance. This strategy allows for continuous, monitoring of the rotational state while maintaining atomic confinement. The method is based on dispersive coupling between atoms and a high-finesse optical cavity mode, such that collective atomic dynamics are encoded in observable properties of the intracavity light field [5]. At the same time, cavity-mediated radiation-pressure effects provide a route to coherently influence the atomic motion, enabling feedback-based control. Compared to previously used approaches, this technique achieves an improvement in rotational sensitivity of roughly three orders of magnitude [38]. In addition to its metrological advantages, the same light–matter interaction supports the emergence of optomechanical entanglement between optical and matter-wave degrees of freedom, thereby opening new possibilities for manipulating persistent superfluid currents [5, 38].

Building on these recent developments, we explore the emergence of quantum correlations in a system of coupled optical cavities incorporating ring-shaped BECs. The setup consists of two cavities linked through photon tunneling, each hosting a condensate confined in a toroidal potential and prepared in a persistent current state. One of the cavities is coherently driven by two degenerate optical modes with opposite orbital angular momentum (OAM), giving rise to an effective angular optical lattice that interacts with the condensate's azimuthal degrees of freedom. We derive the linearized equations governing the system dynamics and evaluate steady-state quantum fluctuations using continuous-variable criteria. The presence of both bipartite and multipartite entanglement involving the cavity fields and collective atomic excitations is systematically investigated as a function of key experimental parameters, such as cavity detuning, intercavity photon coupling, OAM, and thermal effects. Our analysis reveals that OAM serves as an efficient control knob for tailoring quantum correlations and mediating entanglement between spatially separated condensates, underscoring the promise of coupled cavity–BEC platforms for the realization of scalable quantum network architectures.

The structure of the paper is as follows. In Sec. II, we describe the physical model and derive the corresponding Hamiltonian. The main theoretical results are presented and analyzed in Sec. III. Concluding remarks and perspectives for future work are provided in Sec. IV.

II. MODEL AND HAMILTONIAN

We consider the two-cavity configuration depicted in Fig. 1. At the core of the setup is a BEC of alkali atoms, such as sodium, confined within a ring-shaped trapping potential. The toroidal trap is placed symmetrically at the center of each optical cavity and can be realized using well-established experimental methods [39–42].

For an individual atom of mass m, the confining potential expressed in cylindrical coordinates (ρ, z) is given by

$$U(\rho,z)=\frac{1}{2}m\omega_\rho^2(\rho-R)^2+\frac{1}{2}m\omega_z^2z^2, \tag{1}$$

where R denotes the characteristic radius of the torus, while ω_ρ and ω_z represent the trapping frequencies in the radial and axial directions, respectively.

This geometry effectively decouples the azimuthal angle ϕ from the radial and axial motion. We further assume that the condensate occupies the ground state associated with the radial and axial confinements during the entire dynamics, such that the system's nontrivial evolution is restricted to the azimuthal degree of freedom, which experiences no external trapping.

For experimentally realistic parameters, the dynamics along the azimuthal direction can be accurately described within an effective one-dimensional framework [42]. This approximation remains valid even in situations where residual three-dimensional effects are present [20, 43, 44]. The one-dimensional regime is attained provided that the total number of atoms n satisfies the condition [41]

$$n<\frac{4\sqrt{\pi}R}{3a_{\rm na}}\left(\frac{\omega_\rho}{\omega_z}\right)^{1/2}, \tag{2}$$

where $a_{\rm na}$ denotes the s-wave scattering length of sodium atoms.

Manipulation of the condensate is achieved by coupling it to coherent optical fields supported by the cavity. These fields originate from a common laser source and are tuned to the same frequency, but possess opposite OAM $\pm l\hbar$. Their superposition generates a periodically modulated intensity profile along the azimuthal direction, forming an angular optical lattice, as observed experimentally [45]. By detuning the fields to the blue side of the relevant atomic transition, dissipative processes such as absorption and spontaneous emission are strongly suppressed, leaving conservative dipole (AC Stark) interactions as the primary coupling mechanism.

The kinetic energy associated with the rotational motion of the atoms is given by

$$H_{\rm R,K}=-\frac{\hbar}{2I_a}\int_0^{2\pi}\psi^\dagger(\phi)\,\frac{d^2}{d\phi^2}\,\psi(\phi)\,d\phi, \tag{3}$$

where I_a denotes the atomic moment of inertia about the cavity axis.

To describe the atomic field, we adopt the mode expansion

$$\psi(\phi)=\frac{e^{iL_p\phi}}{\sqrt{2}}\,c_p+\frac{e^{i(L_p+2l)\phi}}{\sqrt{2}}\,c_+ +\frac{e^{i(L_p-2l)\phi}}{\sqrt{2}}\,c_-, \tag{4}$$

$$\psi^\dagger(\phi)=\frac{e^{-iL_p\phi}}{\sqrt{2}}\,c_p^\dagger+\frac{e^{-i(L_p+2l)\phi}}{\sqrt{2}}\,c_+^\dagger+\frac{e^{-i(L_p-2l)\phi}}{\sqrt{2}}\,c_-^\dagger \tag{5}$$

TABLE I. Model parameters and symbols used in our numerical simulations.

Symbol	Meaning	Value used / definition
m	atomic mass	$m = 23$ amu
R	ring radius	$R = 12$ μm
ω_ρ	radial trap frequency	$\omega_\rho/2\pi = 42$ Hz
ω_z	axial trap frequency	$\omega_z/2\pi = 42$ Hz
$U(\rho, z)$	trap potential	$U(\rho,z) = \frac{1}{2}m\omega_\rho(\rho - R)^2 + \frac{1}{2}m\omega_z z^2$
n	atom number	$n = 10^4$
L_p	winding number	$L_p = 1$
I_a	moment of inertia	$I_a = mR^2$
g	1D interaction strength	$g = \dfrac{2\hbar\omega_\rho a_{\mathrm{Na}}}{R}$
l	OAM (topological charge)	lattice term $\propto \cos^2(l\phi)$
ω_o	cavity resonance frequency	$\omega_o/2\pi = 10^{15}$ Hz
γ_o	cavity linewidth	$\gamma_o/2\pi = 2$ MHz
P_{in}	input drive power	$P_{\mathrm{in}} = 12.4$ fW
η_{lc}	drive amplitude	$\eta_{lc} = \sqrt{P_{\mathrm{in}}\gamma_o/(\hbar\omega_o)}$
Δ_a	atom-light detuning	$\Delta_a/2\pi = 4.7$ GHz
U_0	single-photon light shift	$u_0 = g_a^2/\Delta_a$
$\tilde{\Delta}$	effective cavity detuning	$\tilde{\Delta} = \Delta_o - u_0 n/2$
ω_c	upper side-mode frequency	$\omega_c = \dfrac{\hbar(L_p + 2l)^2}{2I}$
ω_d	lower side-mode frequency	$\omega_d = \dfrac{\hbar(L_p - 2l)^2}{2I}$
G	linearized coupling constant	$G = \dfrac{u_0\sqrt{n}}{2\sqrt{2}}$; $G/2\pi = 7.5$ kHz
γ_m	side-mode damping	$\gamma_m/2\pi = 0.8$ Hz
Δ_0	radiation-pressure-shifted detuning	-
T	temperature	$T = 10$ nK

Substituting this ansatz into the rotational kinetic Hamiltonian yields

$$H_{\mathrm{R,K}} = \frac{\pi\hbar^2}{2I_a}\Big[L_p^2\, c_p^\dagger c_p + (L_p + 2l)^2\, c_+^\dagger c_+ + (L_p - 2l)^2\, c_-^\dagger c_-\Big]. \tag{6}$$

Introducing collective excitation operators through

$$\sqrt{n}\, c = c_p^\dagger c_+, \qquad \sqrt{n}\, d = c_p^\dagger c_-,$$

the kinetic Hamiltonian can be recast as

$$H_{\mathrm{R,K}} = \frac{\hbar^2(L_p + 2l)^2}{2I_a}\, c^\dagger c + \frac{\hbar^2(L_p - 2l)^2}{2I_a}\, d^\dagger d. \tag{7}$$

We identify these excitations as particle-like modes of the condensate with frequencies

$$\omega_c = \frac{\hbar(L_p + 2l)^2}{2I_a}, \qquad \omega_d = \frac{\hbar(L_p - 2l)^2}{2I_a},$$

such that the kinetic energy takes the compact form

$$H_{\mathrm{R,K}} = \hbar\omega_c c^\dagger c + \hbar\omega_d d^\dagger d. \tag{8}$$

The interaction between the atoms and the cavity-generated angular lattice is described by

$$H_{\mathrm{A,L}} = \int_0^{2\pi} \psi^\dagger(\phi)\, \hbar u_0 \cos^2(l\phi)\, a^\dagger a\, \psi(\phi)\, d\phi. \tag{9}$$

Applying the same mode expansion leads to

$$H_{\mathrm{A,L}} = \frac{\hbar u_0 n}{2}\, a^\dagger a + \frac{\hbar u_0}{4}\, a^\dagger a\Big(c_p^\dagger c_+ + c_+^\dagger c_p + c_p^\dagger c_- + c_-^\dagger c_p\Big). \tag{10}$$

Expressing this Hamiltonian in terms of the collective operators defined above, we obtain

$$H_{\mathrm{A,L}} = \frac{\hbar u_0 n}{2} a^\dagger a + \frac{\hbar u_0\sqrt{2n}}{4} a^\dagger a\, x_c + \frac{\hbar u_0\sqrt{2n}}{4} a^\dagger a\, x_d, \tag{11}$$

where the position quadratures are defined as $\sqrt{2}\, x_c = c^\dagger + c$ and $\sqrt{2}\, x_d = d^\dagger + d$.

Atomic collisions are incorporated through the contact interaction

$$H_{\mathrm{Int}} = \frac{g}{2}\int_0^{2\pi} \psi^\dagger(\phi)\psi^\dagger(\phi)\psi(\phi)\psi(\phi)\, d\phi, \tag{12}$$

with g characterizing the interaction strength.

Using the truncated mode expansion and collective operators, this term reduces to

$$H_{\rm Int} = \hbar g' \Big[n^2 - n + c^\dagger c c^\dagger c - c^\dagger c + d^\dagger d d^\dagger d - d^\dagger d + 4n(c^\dagger c + d^\dagger d) + 2n(cd^\dagger + c^\dagger d) + 4c^\dagger c d^\dagger d \Big]. \tag{13}$$

Expressed in terms of the quadrature variables $\sqrt{2}X_j = j^\dagger + j$ and $\sqrt{2}Y_j = i(j^\dagger - j)$ with $j = c, d$, the interaction Hamiltonian becomes

$$\begin{aligned} H_{\rm Int} = \hbar g' \Big[& N(X_c + iY_c)(X_d + iY_d) + \text{h.c.} \\ & + 2N(X_c^2 + Y_c^2 - 1) + (X_d^2 + Y_d^2 - 1) \\ & + (X_c^2 + Y_c^2 - 1)(X_d^2 + Y_d^2 - 1) \\ & + \frac{1}{4}(X_c^2 + Y_c^2 - 1)(X_c^2 + Y_c^2 - 3) \\ & + \frac{1}{4}(X_d^2 + Y_d^2 - 1)(X_d^2 + Y_d^2 - 3) \Big]. \end{aligned} \tag{14}$$

The effective interaction strength is given by

$$g' = \frac{\omega_\rho a_{na} n_a}{2\pi R}, \tag{15}$$

where ω_ρ is the radial trapping frequency, R denotes the torus radius, and a_{na} is the s-wave scattering length for sodium atoms.

In the frame co-rotating with the driving laser, the effective description of the azimuthal dynamics of the condensate reduces to a one-dimensional interacting many-body Hamiltonian [46, 47]. The total Hamiltonian of the system reads

$$\begin{aligned} H = \sum_{i=1}^{2} \Bigg[& -\frac{\hbar}{2I_{ai}} \int_0^{2\pi} \psi_i^\dagger(\phi_i) \frac{d^2}{d\phi_i^2} \psi_i(\phi_i)\, d\phi_i \\ & + \int_0^{2\pi} \psi_i^\dagger(\phi_i)\, \hbar u_{0i} \cos^2(l\phi_i)\, a_i^\dagger a_i\, \psi_i(\phi_i)\, d\phi_i \\ & + \frac{g_i}{2} \int_0^{2\pi} \psi_i^\dagger(\phi_i) \psi_i^\dagger(\phi_i) \psi_i(\phi_i) \psi_i(\phi_i)\, d\phi_i - \hbar\Delta_{0i} a_i^\dagger a_i \Bigg] \\ & + \hbar J(a_1^\dagger a_2 + a_1 a_2^\dagger) - i\hbar\eta_{lc}(a_i - a_i^\dagger). \end{aligned} \tag{16}$$

As outlined earlier and illustrated schematically in Fig. 1, the hybrid platform under consideration consists of several mutually coupled components. Specifically, photons confined in optical cavities interact with ring-shaped BECs carrying quantized angular momentum and trapped in toroidal potentials [38]. Each cavity is driven by a pair of degenerate modes with opposite OAM $\pm l\hbar$, whose interference produces an angular optical lattice that couples directly to the azimuthal motion of the condensate.

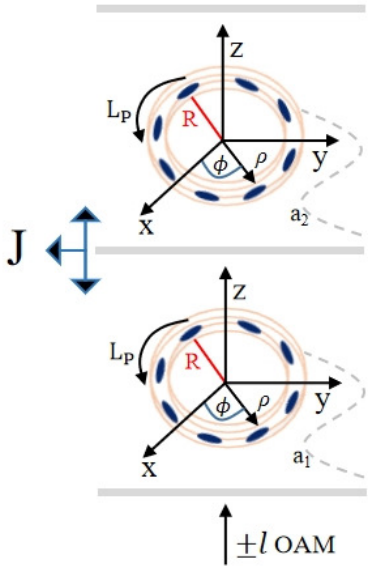

FIG. 1. Schematic of the double-cavity system. Two optical cavities are coupled via photon hopping with rate J. Each cavity contains a Bose-Einstein condensate (BEC) confined in a toroidal (ring) trap of radius R and prepared in a circulating state with winding number L_p. The first cavity is driven (probed) by two optical modes carrying opposite OAM $\pm l\hbar$.

To proceed, we introduce the canonical quadratures for the collective atomic excitation modes appearing in Eqs. (8) and (11),

$$x_{ci} = \frac{c_i^\dagger + c_i}{\sqrt{2}}, \qquad y_{ci} = \frac{c_i - c_i^\dagger}{i\sqrt{2}}, \tag{17}$$

$$x_{di} = \frac{d_i^\dagger + d_i}{\sqrt{2}}, \qquad y_{di} = \frac{d_i - d_i^\dagger}{i\sqrt{2}}. \tag{18}$$

Combining the rotational kinetic energy $H_{\rm R,K}$, the atom–lattice interaction $H_{\rm A,L}$, and the collision-induced interaction term $H_{\rm Int}$, the total effective Hamiltonian can be written as

$$\begin{aligned} \mathcal{H} = \sum_{i=1}^{2} \Bigg[& \frac{\hbar\omega_{ci}}{2} \left(x_{ci}^2 + y_{ci}^2\right) + \frac{\hbar\omega_{di}}{2} \left(x_{di}^2 + y_{di}^2\right) \\ & + \hbar G\, x_{ci} a_i^\dagger a_i + \hbar G\, x_{di} a_i^\dagger a_i \\ & + 2\hbar g_i' n_i \left(x_{ci}^2 + y_{ci}^2\right) + 2\hbar g_i' n_i \left(x_{di}^2 + y_{di}^2\right) \\ & + 2\hbar g_i' n_i \left(x_{ci} x_{di} - y_{ci} y_{di}\right) - \hbar\tilde{\Delta}_i a_i^\dagger a_i \Bigg] \\ & + \hbar J(a_1^\dagger a_2 + a_1 a_2^\dagger) + i\hbar\eta_{lc}(a^\dagger - a). \end{aligned} \tag{19}$$

In Eq. (19), the driving amplitude is defined as

$$\eta_{lc} = \sqrt{\frac{P_{\rm in}\,\gamma_0}{\hbar\omega_0}}, \tag{20}$$

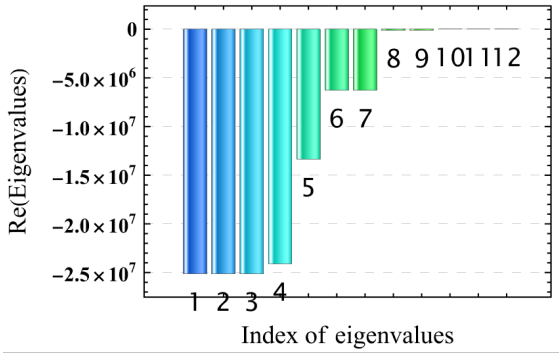

FIG. 2. Re Eigenvalues of the drift matrix $\mathcal{Z}$ as a function of the index Eigenvalues. The parameters are given in Table:1

where $P_{\rm in}$ denotes the input laser power and γ_0 is the cavity decay rate.

Within the Bogoliubov framework, the excitation frequencies are renormalized due to two-body atomic interactions, leading to the modified expressions

$$\omega'_{ci} = \sqrt{\omega_{ci}\big(\omega_{ci} + 4g'_i n_i\big)}, \qquad \omega'_{di} = \sqrt{\omega_{di}\big(\omega_{di} + 4g'_i n_i\big)}, \tag{21}$$

where the effective interaction parameter is given by

$$g'_i = \frac{g_i}{4\pi\hbar}, \qquad g_i = \frac{2\hbar\omega_\rho a_{\rm na}}{R}. \tag{22}$$

Here, $a_{\rm na}$ is the s-wave scattering length of sodium atoms, ω_ρ is the radial trapping frequency, and R denotes the radius of the toroidal trap.

The interaction between the condensate side modes and the cavity field originates from the angular optical lattice and is characterized by the coupling strength

$$G_i = \frac{u_{0i}\sqrt{n_i}}{2\sqrt{2}}, \qquad u_{0i} = \frac{g_{ai}^2}{\Delta_{ai}}, \tag{23}$$

where g_{ai} represents the single-atom–single-photon coupling constant and Δ_{ai} is the detuning between the cavity field and the relevant atomic transition. The corresponding quadrature operators for the side modes are defined following Ref. [38].

In addition, the cavity detuning appearing in Eq. (16) is defined as

$$\Delta_{0i} = \omega_l - \omega_{0i}, \tag{24}$$

with ω_l and ω_{0i} denoting the laser and cavity resonance frequencies, respectively. The operators a_i and $a_i^\dagger$ describe the annihilation and creation of photons in the ith cavity mode.

To account for dissipation and quantum fluctuations, we employ the Heisenberg–Langevin formalism [48]. Starting from the total Hamiltonian in Eq. (19), the equations of motion are linearized around the steady-state solutions by expressing each operator as the sum of its mean value and a small fluctuation, i.e.,

$$\begin{aligned} x_c &= x_c^{(s)} + \Delta x_c, \qquad & y_c &= y_c^{(s)} + \Delta y_c, \\ x_d &= x_d^{(s)} + \Delta x_d, \qquad & y_d &= y_d^{(s)} + \Delta y_d, \\ a &= a^{(s)} + \Delta a. \end{aligned} \tag{25}$$

The resulting linearized fluctuation equations take the form

$$\dot{x}_{ci} = \big(\omega_{ci} + 4g'_i n_i\big) y_{ci} - 2g'_i n_i y_{di}, \tag{26}$$

$$\dot{y}_{ci} = -\big(\omega_{ci} + 4g'_i n_i\big) x_{ci} - G_i a_i^\dagger a_i - 2g'_i n_i x_{di}, \tag{27}$$

$$\dot{x}_{di} = \big(\omega_{di} + 4g'_i n_i\big) y_{di} - 2g'_i n_i y_{ci}, \tag{28}$$

$$\dot{y}_{di} = -\big(\omega_{di} + 4g'_i n_i\big) x_{di} - G_i a_i^\dagger a_i - 2g'_i n_i x_{ci}, \tag{29}$$

and for the cavity fields,

$$\begin{aligned} \dot{a}_1 = &-\frac{\gamma_{01}}{2} a_1 + i\big[\tilde{\Delta}_1 - G_1(x_{c1} + x_{d1})\big] a_1 - iJa_2 + \eta_{lc} \\ &+\sqrt{\mu\gamma_{01}}\, a_1^{(\rm in)}, \end{aligned} \tag{30}$$

$$\begin{aligned} \dot{a}_2 = &-\frac{\gamma_{02}}{2} a_2 + i\big[\tilde{\Delta}_2 - G_2(x_{c2} + x_{d2})\big] a_2 - iJa_1 \\ &+\sqrt{\mu\gamma_{02}}\, a_2^{(\rm in)}. \end{aligned} \tag{31}$$

In Eqs. (20)–(25), the operators ϵ_c, ϵ_d, and $a^{(\rm in)}$ represent the input noise terms associated with the atomic side modes and the cavity fields, respectively. Finally, the effective detuning for a cavity containing a condensate is defined as

$$\Delta_i = \tilde{\Delta}_{ai} - G_i x_{cis} - G_i x_{dis}. \tag{32}$$

The mean thermal occupation numbers of the condensate side modes at equilibrium are given by

$$N_{ci}(\omega_{ci}) = \left[\exp\left(\frac{\hbar\omega_{ci}}{k_B T_{ai}}\right) - 1\right]^{-1}, \tag{33}$$

$$N_{di}(\omega_{di}) = \left[\exp\left(\frac{\hbar\omega_{di}}{k_B T_{ai}}\right) - 1\right]^{-1}, \tag{34}$$

where k_B denotes the Boltzmann constant and T_{ai} represents the effective temperature of the atomic environment.

To describe the quantum fluctuations, we introduce the cavity-field quadratures

$$\sqrt{2}\,\delta x_a = \delta a + \delta a^\dagger, \qquad \sqrt{2}\,\delta y_a = i(\delta a^\dagger - \delta a). \tag{35}$$

Substituting these definitions into Eqs. (20)–(25), the linearized Langevin equations for the fluctuations can be cast into the compact matrix form

$$\dot{u}(t) = \mathcal{Z} u(t) + v(t), \tag{36}$$

where the individual components explicitly satisfy

$$\delta\dot{x}_{ci} = (\omega_{ci} + 4g'_i n_i)\delta y_{ci} - 2g'_i n_i \delta y_{di}, \tag{37}$$

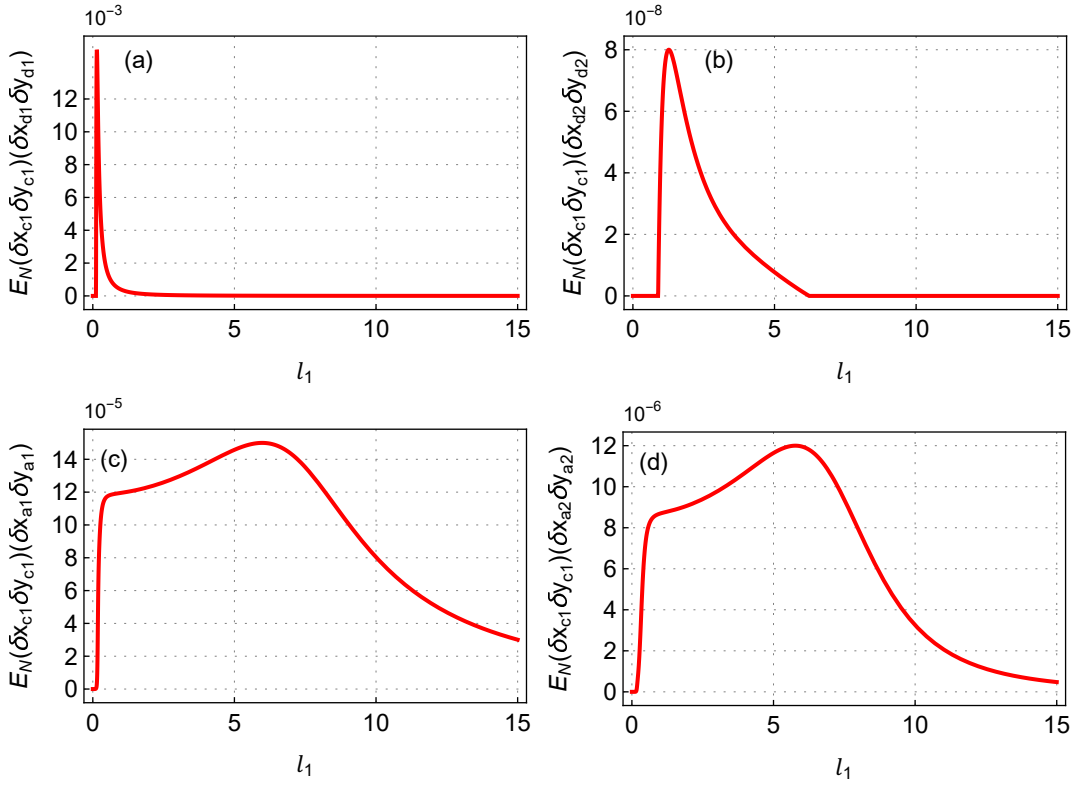

FIG. 3. Bipartite entanglement E_N as a function of the OAM l_1 for different mode pairs: (a) atomic modes x_{c1} and x_{d1}, (b) atomic modes x_{c1} and x_{d2}, (c) atomic mode x_{c1} and cavity mode x_{a1}, and (d) atomic mode x_{c1} and cavity mode x_{a2}. The parameters are chosen as $l_2 = 10$ (dimensionless), $L_{p1} = L_{p2} = 1$ (dimensionless), $J = 0.2\,\gamma_{01}$, atomic mass $m = 3.82\times10^{-26}$ kg, cavity decay rates $\gamma_{01} = \gamma_{02} = 2\pi \times 10^6$ Hz, radial trap frequency $\omega_\rho = 2\pi \times 42$ Hz, input laser power $P_{\rm in} = 12.4 \times 10^{-15}$ W, and optomechanical coupling strengths $G_1 = G_2 = 2\pi \times 7.5 \times 10^3$ Hz. All remaining parameters are identical to those listed in Table I.

$$\delta\dot{y}_{ci} = -(\omega_{ci} + 4g_i' n_i)\delta x_{ci} + G_{ri}\delta y_{ai} - 2g_i' n_i \delta x_{di} - \gamma_{mi}\delta y_{ci} + \epsilon_{ci}, \tag{38}$$

$$\delta\dot{x}_{di} = (\omega_{di} + 4g_i' n_i)\delta y_{di} - 2g_i' n_i \delta y_{ci}, \tag{39}$$

$$\delta\dot{y}_{di} = -(\omega_{di} + 4g_i' n_i)\delta x_{di} + G_{ri}\delta y_{ai} - 2g_i' n_i \delta x_{ci} - \gamma_{mi}\delta y_{di} + \epsilon_{di}, \tag{40}$$

and for the cavity quadratures,

$$\delta\dot{x}_{a1} = -\Delta_1 \delta y_{a1} - \frac{\gamma_{01}}{2}\delta x_{a1} - G_{r1}(\delta x_{c1} + \delta x_{d1}) + J\delta y_{a2} + \sqrt{\gamma_{01}}\,\delta x_{a1}^{\rm in}, \tag{41}$$

$$\delta\dot{y}_{a1} = \Delta_1 \delta x_{a1} - \frac{\gamma_{01}}{2}\delta y_{a1} - J\delta x_{a2} + \sqrt{\gamma_{01}}\,\delta y_{a1}^{\rm in}, \tag{42}$$

$$\delta\dot{x}_{a2} = -\Delta_2 \delta y_{a2} - \frac{\gamma_{02}}{2}\delta x_{a2} - G_{r2}(\delta x_{c2} + \delta x_{d2}) + J\delta y_{a1} + \sqrt{\gamma_{02}}\,\delta x_{a2}^{\rm in}, \tag{43}$$

$$\delta\dot{y}_{a2} = \Delta_2 \delta x_{a2} - \frac{\gamma_{02}}{2}\delta y_{a2} - J\delta x_{a1} + \sqrt{\gamma_{02}}\,\delta y_{a2}^{\rm in}. \tag{44}$$

Here, the effective optomechanical coupling is defined as

$$G_{ri} = i\sqrt{2}Ga_{is}, \tag{45}$$

with steady-state cavity amplitudes

$$a_{1s} = \frac{2(\gamma_{02} - 2i\Delta_2)\eta_{lc}}{4J^2 + \gamma_{01}\gamma_{02} - 2i(\gamma_{02}\Delta_1 + \gamma_{01}\Delta_2) - 4\Delta_1\Delta_2}, \tag{46}$$

$$a_{2s} = \frac{-4iJ\eta_{lc}}{4J^2 + \gamma_{01}\gamma_{02} - 2i(\gamma_{02}\Delta_1 + \gamma_{01}\Delta_2) - 4\Delta_1\Delta_2}. \tag{47}$$

The fluctuation vector and noise vector in Eq. (29) are defined as

$$u(t) = [\delta x_{ci}, \delta y_{ci}, \delta x_{di}, \delta y_{di}, \delta x_{ai}, \delta y_{ai}]^T, \tag{48}$$

$$v(t) = [0, \epsilon_{ci}, 0, \epsilon_{di}, \sqrt{\gamma_{0i}}\delta x_{ai}^{\rm in}, \sqrt{\gamma_{0i}}\delta y_{ai}^{\rm in}]^T. \tag{49}$$

The drift matrix $\mathcal{Z}$ follows directly from the coefficients

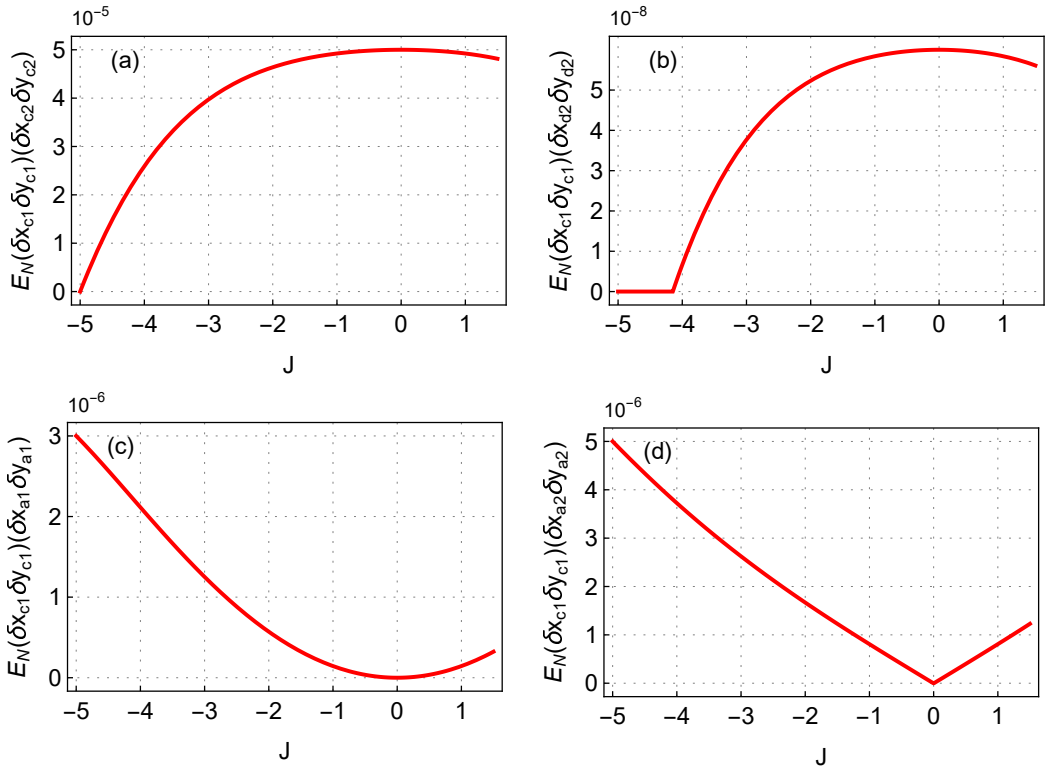

FIG. 4. Bipartite entanglement E_N of different modes vs Photon hopping J (a) atomic mode x_{c1} and x_{d1} (b) atomic mode x_{c1} and x_{d2} (c) atomic mode x_{c1} and cavity mode x_{a1} (d) atomic mode x_{c1} and cavity mode x_{a2}. With $l_1 = 100$, $l_2 = 10$. All the parameters are same in Fig.3.

of the linearized equations and has the general structure

$$\mathcal{Z} = \begin{pmatrix} a_{11} & a_{12} & \cdots & a_{1,12} \\ a_{21} & a_{22} & \cdots & a_{2,12} \\ \vdots & \vdots & \ddots & \vdots \\ a_{12,1} & a_{12,2} & \cdots & a_{12,12} \end{pmatrix}.$$

System stability is ensured by choosing the steady-state cavity amplitudes to be real and verifying that the real parts of all eigenvalues of $\mathcal{Z}$ are negative. Assuming Gaussian quantum noise with vanishing mean, the steady state of the fluctuations corresponds to a continuous-variable Gaussian state fully characterized by the covariance matrix V, whose elements are defined as

$$V_{ij} = \frac{1}{2}\langle u_i(t)u_j(t') + u_j(t')u_i(t)\rangle. \tag{50}$$

For a stable system, V satisfies the Lyapunov equation

$$\mathcal{Z}V + V\mathcal{Z}^T + D = 0, \tag{51}$$

where the diffusion matrix D is diagonal and takes the form

$$D = \mathrm{diag}[0, -\gamma_{m1}(2N_{c1}+1), 0, -\gamma_{m2}(2N_{d1}+1), 0, -\gamma_{m1}(2N_{c2}+1), 0, -\gamma_{m2}(2N_{d2}+1), -\gamma_{01}/2, -\gamma_{01}/2, -\gamma_{02}/2, -\gamma_{02}/2]\,. \tag{52}$$

The Lyapunov equation is solved numerically; however, owing to the high dimensionality of the resulting covariance matrix, its explicit analytical form is not reported. To characterize quantum correlations between different subsystems, we adopt the logarithmic negativity [49], a standard quantifier of bipartite entanglement. This measure is defined as

$$E_n = \max[0, -\ln(2\eta')]\,, \tag{53}$$

where η' denotes the smallest symplectic eigenvalue of the partially transposed reduced covariance matrix associated with the two subsystems under consideration, obtained as $\eta' = \min \mathrm{eig}\left|i\Omega_2\tilde{V}_4\right|$.

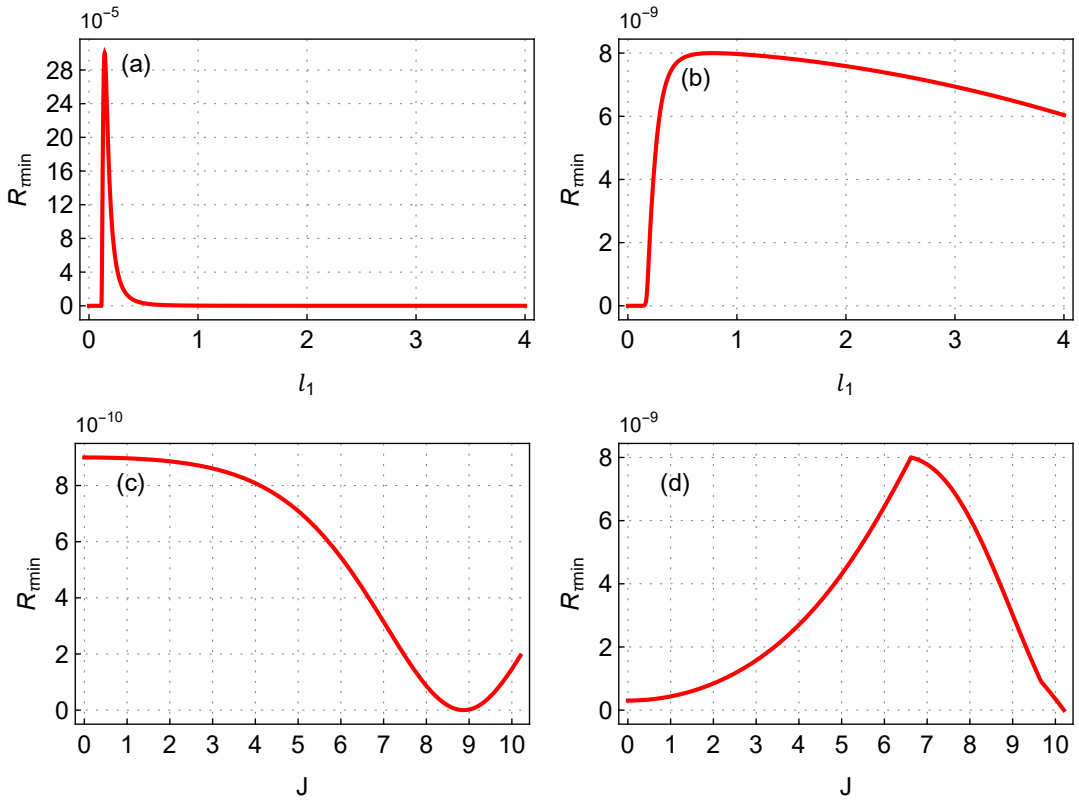

FIG. 5. Tripartite entanglement $R_{\tau\min}$ of different modes vs OAM l_1 and photon hopping J. (a) atomic mode x_{c1},x_{d1}, and x_{d2} (b) x_{c2}, x_{d1}, and x_{a1} with $J = 0.2\gamma_{01}$ (c) atomic mode x_{c1},x_{d1}, and x_{d2} (d) x_{c2}, x_{d1}, and x_{a1} with $l_1 = 100$. All the parameters are same in Fig.3.

In addition to bipartite correlations, our primary focus is on the emergence of genuine tripartite entanglement. To this end, we employ the residual contangle R_τ [50, 51], which provides a reliable quantifier of multipartite entanglement in continuous-variable systems.

For Gaussian states, genuine three-mode entanglement can be assessed using the minimum residual contangle, as introduced in Ref. [52]. This approach relies on the contangle, defined as the square of the logarithmic negativity, evaluated across all possible bipartitions of the system.

Specifically, for a three-mode Gaussian state, the entanglement between one mode and the remaining pair is determined by performing partial transposition on the corresponding covariance matrix and extracting the smallest symplectic eigenvalue. The contangle is then computed for each of the three inequivalent bipartitions. The genuine tripartite contribution is identified by selecting the minimum of these three bipartite contangles, rather than subtracting pairwise correlations. For the present system, this quantity can be written explicitly as

$$R_\tau^{\min}(x_{ci}, x_{di}, a_i) = \min\left[R_\tau^{x_{ci}|x_{di},a_i}, R_\tau^{x_{di}|x_{ci},a_i}, R_\tau^{a_i|x_{ci},x_{di}}\right]. \tag{54}$$

III. Results and discussion

Using experimentally realistic parameters [38, 53–55], we investigate the emergence and control of quantum correlations in the proposed coupled cavity–BEC system.

A. Stability analysis: eigenvalues of the drift matrix

The dynamical stability of the linearized system is examined by analyzing the real parts of the eigenvalues of the drift matrix $\mathcal{Z}$. Figure 2 shows the spectrum of these eigenvalues as a function of their index for the parameter set summarized in Table I. The eigenvalue distribution provides a direct criterion for assessing the stability of the steady state governed by the quantum Langevin equations.

The stability confirmed in Fig. 2 validates the linearized Heisenberg–Langevin treatment and ensures that the covariance matrix obtained from the Lyapunov equation is well defined. This provides a solid foundation for the quantitative analysis of bipartite and multipartite entanglement presented in the subsequent sections.

B. Bipartite entanglement versus OAM

Figure 3 shows the dependence of the bipartite entanglement E_N on the OAM l_1 for several combinations of atomic and cavity modes. The four panels correspond to

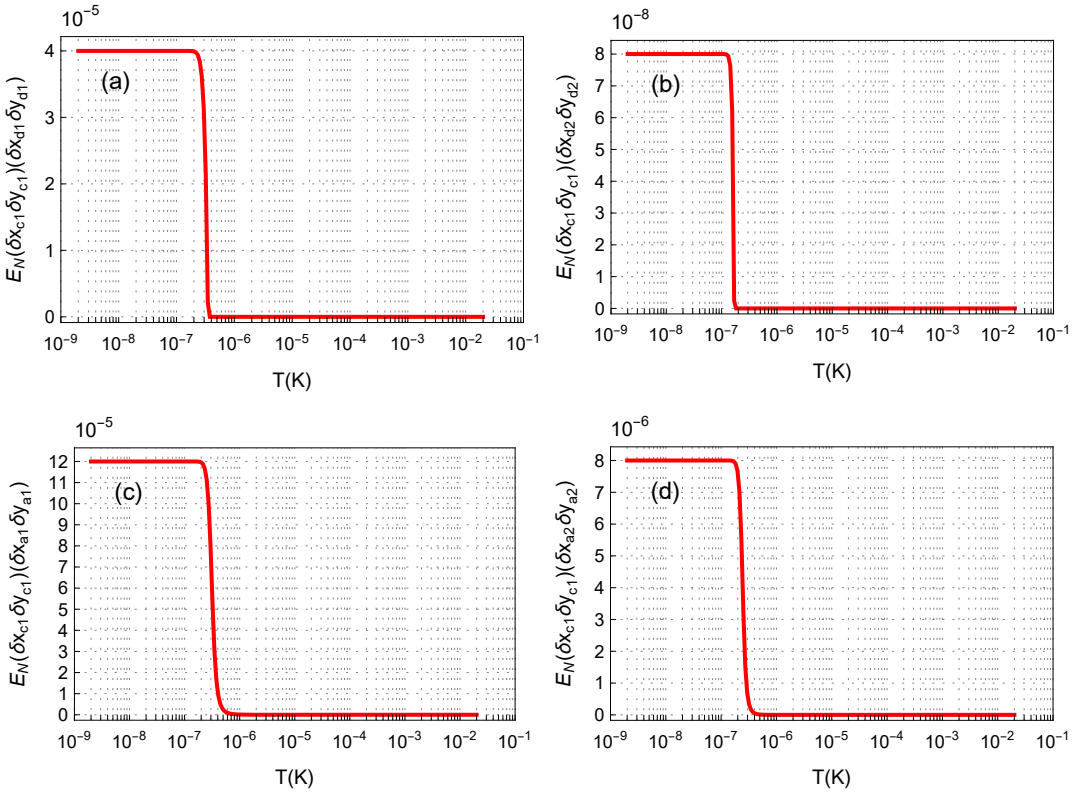

FIG. 6. Bipartite entanglement E_N as a function of temperature T for different mode pairs: (a) atomic modes x_{c1} and x_{d1}, (b) atomic modes x_{c1} and x_{d2}, (c) atomic mode x_{c1} and cavity mode x_{a1}, and (d) atomic mode x_{c1} and cavity mode x_{a2}. The parameters are chosen as $l_2 = 10$ (dimensionless), $L_{p1} = L_{p2} = 1$ (dimensionless), $J = 0.2\,\gamma_{01}$, atomic mass $m = 3.82\times10^{-26}$ kg, cavity decay rates $\gamma_{01} = \gamma_{02} = 2\pi\times10^{6}$ Hz, radial trapping frequency $\omega_\rho = 2\pi\times42$ Hz, input laser power $P_{\rm in} = 12.4\times10^{-15}$ W, and optomechanical coupling strengths $G_1 = G_2 = 2\pi\times7.5\times10^{3}$ Hz. All remaining parameters are the same as those listed in Table I.

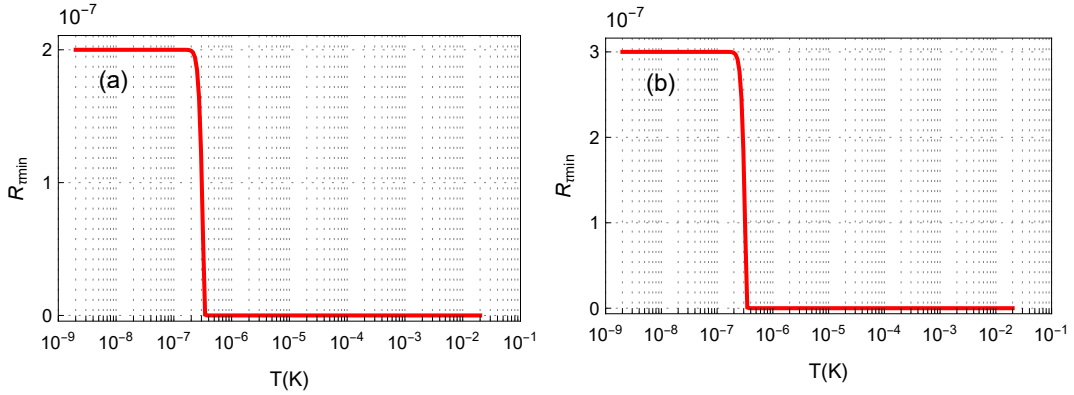

FIG. 7. Tripartite entanglement $R_{\tau\rm min}$ of different modes vs temperature T. (a) atomic mode x_{c1},x_{d1}, and x_{d2} (b) x_{c2}, x_{d1}, and x_{a1}. All the parameters are same in Fig.3.

the entanglement between (a) the two atomic side modes of the first ring, x_{c1} and x_{d1}; (b) the atomic mode of the first ring, x_{c1}, and the side mode of the second ring, x_{d2}, belonging to different condensates; (c) the atomic mode of the first ring, x_{c1}, and the first cavity mode, x_{a1}; and (d) the atomic mode of the first ring, x_{c1}, and the second cavity mode, x_{a2}.

As illustrated in Fig. 3(a), the entanglement between the two side modes of the same condensate is maximal for small values of l_1 and decreases rapidly as l_1 increases. This trend can be attributed to the enhanced spatial overlap and stronger interactions at low OAM, whereas

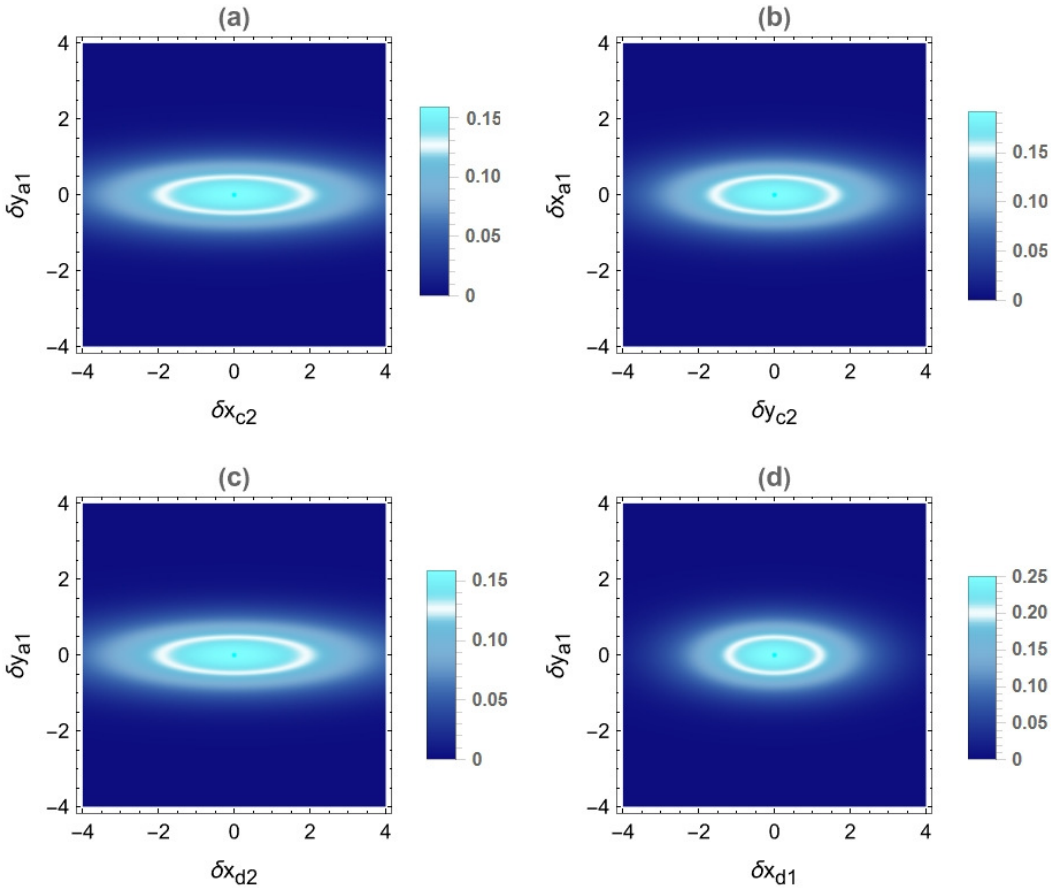

FIG. 8. Wigner function of the different modes of the two cavities. All the parameters are same in Fig.3.

higher l_1 values lead to reduced effective coupling due to the increasing separation of rotational energy levels.

By contrast, Fig. 3(b) shows that entanglement between atomic modes associated with different condensates appears only within a narrow range of intermediate l_1 values. This behavior reflects the indirect coupling mechanism between the condensates, which is mediated by photon hopping and cavity-induced correlations, making the resulting entanglement weaker and more sensitive to variations in OAM.

Figures 3(c) and 3(d) display a qualitatively different dependence for the hybrid atomic–cavity entanglement. In these cases, the logarithmic negativity initially grows with increasing l_1, reaches a maximum at moderate OAM, and then slowly decreases at larger l_1. The existence of an optimal l_1 indicates a balance between the enhancement of optomechanical coupling provided by the angular lattice and the suppression of coherent dynamics caused by detuning effects at high OAM. Importantly, the atomic–cavity entanglement is found to be more robust than purely atomic correlations, emphasizing the essential role of the optical cavity field in mediating and sustaining quantum entanglement.

C. Bipartite entanglement versus photon hopping

Figure 4 displays the variation of the bipartite entanglement E_N with the photon-hopping amplitude J for the same pairs of modes examined in Fig. 3, with the orbital angular momenta fixed at $l_1 = 100$ and $l_2 = 10$. Since photon hopping governs the transfer of photons between the two cavities, it plays a crucial role in establishing and modifying inter-cavity quantum correlations.

As shown in Fig. 4(a), the entanglement between the atomic side modes of the first ring, x_{c1} and x_{d1}, increases steadily with $|J|$ and eventually reaches a saturation value. This behavior indicates that stronger photon tunneling amplifies the effective interaction between atomic modes through enhanced cavity-mediated coupling. A qualitatively similar dependence is observed in Fig. 4(b) for the atomic modes x_{c1} and x_{d2} belonging to different condensates, although the overall entanglement remains weaker due to the spatial separation between the rings.

Figures 4(c) and 4(d) illustrate the dependence of the entanglement between the atomic mode x_{c1} and the cavity modes x_{a1} and x_{a2} on the photon-hopping strength. In contrast to the purely atomic case, the entanglement in these hybrid configurations decreases as $|J|$ increases, attaining a minimum around $J \approx 0$, and then shows a slight

recovery at larger hopping amplitudes. This nonmonotonic behavior arises from the competition between local atom–cavity interactions and nonlocal photon exchange between the cavities. When photon hopping becomes dominant, correlations tend to spread over the entire system, thereby reducing local atomic–cavity entanglement in favor of more delocalized correlations.

Overall, Fig. 4 emphasizes the dual role of photon hopping as both a mechanism for strengthening and redistributing quantum correlations. By adjusting J, it is possible to control whether entanglement is predominantly localized within individual cavities or shared nonlocally among distant atomic and optical modes.

Taken together, the results presented in Figs. 3 and 4 demonstrate that OAM and photon hopping act as complementary control parameters for tailoring bipartite entanglement in hybrid cavity–BEC platforms. This tunability provides a versatile route toward the realization of controllable quantum networks based on coupled matter–light systems.

D. Tripartite entanglement versus OAM and photon hopping

Figure 5 presents the behavior of the minimum residual contangle $R_{\min}$ as a function of the OAM l_1 and the photon-hopping strength J for different combinations of atomic and cavity modes. The residual contangle quantifies genuine tripartite entanglement, capturing correlations that cannot be reduced to pairwise contributions.

In Fig. 5(a), where the tripartite entanglement among the first ring condensate atomic modes x_{c1} as well as x_{d1}, and second ring condensate atomic mode x_{d2} is shown as a function of l_1, a pronounced peak appears at small OAM. As l_1 increases, $R_{\min}$ rapidly decreases and eventually vanishes. This behavior indicates that genuine tripartite correlations among atomic modes are favored when the rotational states are closely spaced, while increasing l_1 suppresses collective coherence due to enhanced energy mismatch.

Figure 5(b) illustrates the tripartite entanglement shared between the second condensate atomic mode x_{c2} and the hybrid pair of first atomic condensate and cavity modes x_{d1} and x_{a1} for fixed photon hopping $J = 0.2\gamma_{01}$. In this case, $R_{\min}$ initially increases with l_1, reaches a maximum at intermediate values, and then slowly decreases. This nonmonotonic behavior highlights the competition between orbital-angular-momentum–induced coupling enhancement and detuning-induced suppression of coherent interactions.

The dependence of tripartite entanglement on photon hopping is shown in Figs. 5(c) and 5(d). In Fig. 5(c), for first condensate atomic modes x_{c1} as well as x_{d1} along with second condensate atomic modes x_{d2}, $R_{\min}$ decreases with increasing J, reaching a minimum near intermediate coupling strengths before partially recovering. This indicates that strong photon hopping redistributes correlations away from purely atomic tripartite configurations. Conversely, Fig. 5(d) demonstrates that for hybrid atomic modes for first x_{d1} and second x_{c2} cavity along with first cavity modes tripartite states, $R_{\min}$ increases with J up to an optimal value and then diminishes at larger hopping strengths, reflecting an optimal balance between local atom–cavity coupling and intercavity photon exchange.

In general, Fig. 5 establishes that both OAM and photon hopping act as powerful control parameters to engineer genuine tripartite entanglement, allowing selective enhancement or suppression of multipartite correlations.

E. Bipartite entanglement versus temperature

Figure 6 presents the variation of the bipartite entanglement E_N with temperature for several pairs of atomic and cavity modes. In all cases, the entanglement remains almost unchanged in the ultracold regime and then decreases abruptly once the temperature exceeds a characteristic critical value.

As shown in Figs. 6(a) and 6(b), the entanglement shared between atomic modes survives up to temperatures of the order of 10^{-7} K. Beyond this point, thermal fluctuations become dominant and quickly suppress the quantum correlations. This rapid degradation highlights the strong susceptibility of purely atomic entanglement to thermally induced excitations.

The temperature dependence of hybrid atomic–cavity entanglement is depicted in Figs. 6(c) and 6(d). In contrast to the atomic–atomic case, these hybrid correlations display a moderately improved tolerance to thermal effects, retaining finite values over a wider temperature interval. This enhanced stability originates from the presence of the cavity field, which mediates the interaction and partially protects the atomic degrees of freedom against thermal decoherence.

Altogether, these findings indicate that although increasing temperature eventually eliminates all bipartite entanglement, hybrid atom–photon correlations exhibit greater robustness than their purely atomic counterparts. This underscores the beneficial role of cavity-assisted interactions in sustaining quantum correlations under realistic finite-temperature conditions.

F. Tripartite entanglement versus temperature

Figure 7 depicts the influence of temperature on the minimum residual contangle $R_{\min}$ for two distinct tripartite configurations. In both cases, the tripartite entanglement remains finite at very low temperatures and then collapses abruptly beyond a critical temperature scale.

In Fig. 7(a), which corresponds to tripartite entanglement among atomic modes x_{c1}, x_{d1}, and x_{d2}, $R_{\min}$ exhibits a plateau at ultracold temperatures followed by a sharp transition to zero near $T \sim 10^{-7}$ K. This sudden disappearance highlights the extreme fragility of genuine tripartite atomic entanglement with respect to thermal fluctuations.

Figure 7(b) shows a similar trend for the hybrid tripartite state involving atomic and cavity modes. Although the initial magnitude of $R_{\min}$ is larger than in the purely atomic case, the tripartite entanglement is still destroyed once thermal excitations exceed a critical threshold. The

abrupt nature of this transition reflects the collective character of multipartite correlations, which are more sensitive to noise than bipartite entanglement.

Taken together, Figs. 6 and 7 demonstrate that while both bipartite and tripartite entanglement can be generated and controlled in the coupled cavity–BEC system, maintaining genuine multipartite quantum correlations requires operation deep in the ultracold regime. These findings underline the importance of temperature control in experiments aimed at realizing scalable quantum networks based on hybrid atom–photon platforms.

G. Phase-space representation via Wigner functions

To gain deeper insight into the steady-state properties of the coupled cavity–BEC system, we investigate the phase-space structure of selected modes by reconstructing their corresponding Wigner functions. The Wigner function provides a convenient phase-space representation of quantum fluctuations and allows a direct visualization of squeezing as well as correlations between different quadratures.

For a Gaussian steady state, the Wigner function associated with a given set of fluctuation quadratures is given by

$$W(\psi) = \frac{\exp\left[-\frac{1}{2}\psi V^{-1}\psi^{\mathrm{T}}\right]}{\pi^2\sqrt{\det V}}, \tag{55}$$

where ψ denotes the vector of selected quadrature fluctuations and V is the corresponding reduced covariance matrix obtained from the Lyapunov equation.

Figure 8 shows representative projections of the Wigner functions for different modes of the two coupled cavities. In Fig. 8(a), the phase-space distribution involving the collective atomic mode of the second condensate x_{c2} and the cavity quadrature δy_{a1} is displayed. Figure 8(b) presents the distribution associated with the collective atomic quadrature δy_{c2} and the first cavity quadrature δx_{a1}. In both cases, the Wigner functions exhibit elongated elliptical contours centered at the origin, indicating anisotropic quantum fluctuations induced by the effective atom–cavity coupling. The symmetry of these distributions confirms that the system reaches a stable steady state without any mean-field displacement.

In Fig. 8(c), the Wigner function corresponding to the atomic side mode of the second condensate x_{d2} and the cavity quadrature δy_{a1} is shown. Compared to panels (a) and (b), the phase-space ellipse is more strongly distorted, reflecting a redistribution of fluctuations due to the combined effects of atom–atom interactions within the ring-shaped condensate and cavity-mediated coupling. This behavior highlights the sensitivity of the side modes to OAM dependent interactions.

Figure 8(d) displays the Wigner distribution for the atomic side mode of the first condensate x_{d1} coupled to the first cavity quadrature δy_{a1}. Here, the phase-space distribution is more localized with a higher peak value, indicating a stronger suppression of fluctuations along one quadrature direction. This observation is consistent with the enhanced atom–cavity correlations discussed earlier and demonstrates the role of the optical cavity in shaping the fluctuation dynamics of the condensate modes.

The Wigner function projections in Fig. 8 provide a clear phase-space picture of the steady-state correlations between atomic and cavity degrees of freedom. The elliptical structures observed for different mode combinations illustrate how OAM, atom–atom interactions, and cavity coupling collectively redistribute fluctuations in the hybrid double-ring cavity–BEC system.

IV. Feasibility and Experimental Prospects

Our study holds strong practical relevance for experimental realization in next-generation quantum hybrid systems, particularly in the emerging field of BEC cavity optomagnomechanics. Each subsystem, cavity-BEC coupling [38], cavity magneto-mechanical systems [56], and BEC in toroidal traps [26] has already been experimentally demonstrated with high precision. Integrating these components into a single platform is experimentally feasible using current technologies. YIG coupled to superconducting microwave cavities at cryogenic temperatures provides a mature setup for generating strong photon–magnon–phonon interactions. On the atomic side, toroidally trapped BECs that interact with light-carrying OAM have been implemented using Laguerre–Gaussian modes.

V. Conclusion

We have analyzed quantum correlations in a dual-cavity system containing ring-shaped BECs coupled through photon hopping and angular optical lattices. By employing a linearized quantum Langevin approach, we characterized the steady-state bipartite and tripartite entanglement between collective atomic side modes and cavity fields. Our results demonstrate that OAM and inter-cavity photon coupling provide effective and independent control parameters for tuning both local and nonlocal correlations. We further showed that atom–cavity entanglement is more resilient to thermal effects than purely atomic correlations, while genuine tripartite entanglement survives only in the ultracold regime. Phase-space analysis using Wigner functions corroborates the entanglement behavior and illustrates the redistribution of fluctuations among the coupled modes. These findings identify coupled cavity–ring BEC systems as a controllable platform for engineering steady-state matter–light correlations.

[1] E. Schrödinger, Mathematical Proceedings of the Cambridge Philosophical Society **31**, 555 (1935).
[2] D. Bouwmeester, A. K. Ekert, and A. Zeilinger (2000).
[3] N. Zou, Journal of Physics: Conference Series **1827**, 012120 (2021).
[4] J. S. Bell, Physics Physique Fizika **1**, 195 (1964).
[5] M. Aspelmeyer, T. J. Kippenberg, and F. Marquardt, Rev. Mod. Phys. **86**, 1391 (2014).
[6] D. Vitali, S. Gigan, A. Ferreira, H. Boehm, P. Tombesi, A. Guerreiro, V. Vedral, A. Zeilinger, and M. Aspelmeyer, Phys. Rev. Lett. **98** (2006).
[7] L.-l. Zhai, H.-J. Du, and J.-L. Guo, Quantum Information Processing **22** (2023).
[8] S.-X. Wu, C.-H. Bai, G. Li, C.-S. Yu, and T. Zhang, Optics Express **32** (2023).
[9] C. Jiang, H. Lu, Z. Zhai, and G. Chen, Photonics **9**, 818 (2022).
[10] X. Yang, H. Yin, F. Zhang, and J. Nie, Laser Physics Letters **20**, 015205 (2022).
[11] D. Aoune, B. Noureddine, N. Habiballah, and M. Nassik, International Journal of Modern Physics B **38** (2023).
[12] L. Zigeng, X. Li, and X. Zhong, Optics Express **31** (2023).
[13] L. Youness, B. Maroufi, and M. Daoud, Modern Physics Letters A **38** (2023).
[14] J.-D. Tang, Q.-Z. Cai, C. Ze-di, N. Xu, G.-Y. Peng, P.-Q. Chen, D.-G. Wang, Z.-W. Xia, Y. Wang, H.-Z. Song, Q. Zhou, and D. Guangwei, Physics Letters A **429**, 127966 (2022).
[15] D. Vitali, S. Mancini, and P. Tombesi, Phys. Rev. A **64**, 051401 (2001).
[16] A. A. Geraci, S. B. Papp, and J. Kitching, Phys. Rev. Lett. **105**, 101101 (2010).
[17] P. Fritschel, Advanced Gravitational Wave Detectors , 113 (2012).
[18] R. Riedinger, A. Wallucks, I. Marinkovic, C. Löschnauer, M. Aspelmeyer, S. Hong, and S. Gröblacher, Nature **556** (2018).
[19] S. Barzanjeh, A. Xuereb, S. Groeblacher, M. Paternostro, C. Regal, and E. Weig, Nature Physics **18** (2021).
[20] K. C. Wright, R. B. Blakestad, C. J. Lobb, W. D. Phillips, and G. K. Campbell, Phys. Rev. Lett. **110**, 025302 (2013).
[21] C. Ryu, P. W. Blackburn, A. A. Blinova, and M. G. Boshier, Phys. Rev. Lett. **111**, 205301 (2013).
[22] G. E. Marti, R. Olf, and D. M. Stamper-Kurn, Phys. Rev. A **91**, 013602 (2015).
[23] P. Öhberg and E. M. Wright, Phys. Rev. Lett. **123**, 250402 (2019).
[24] A. L. Fetter, Rev. Mod. Phys. **81**, 647 (2009).
[25] D. Freilich, D. Bianchi, A. Kaufman, T. Langin, and D. Hall, Science **329**, 1182 (2010).
[26] C. Ryu, M. F. Andersen, P. Cladé, V. Natarajan, K. Helmerson, and W. D. Phillips, Phys. Rev. Lett. **99**, 260401 (2007).
[27] N. R. Cooper, Advances in Physics **57**, 539 (2008).
[28] Y. Shin, M. Saba, M. Vengalattore, T. A. Pasquini, C. Sanner, A. E. Leanhardt, M. Prentiss, D. E. Pritchard, and W. Ketterle, Phys. Rev. Lett. **93**, 160406 (2004).
[29] D. R. Tilley, *Superfluidity and superconductivity* (Routledge, 2019).
[30] Z. Mehdi, A. Bradley, J. Hope, and S. Szigeti, SciPost physics **11**, 080 (2021).
[31] S. Pandey, H. Mas, G. Vasilakis, and W. von Klitzing, Phys. Rev. Lett. **126**, 170402 (2021).
[32] L. Amico, M. Boshier, G. Birkl, A. Minguzzi, C. Miniatura, L.-C. Kwek, D. Aghamalyan, V. Ahufinger, D. Anderson, N. Andrei, *et al.*, AVS Quantum Science **3**, https://doi.org/10.1116/5.0026178 (2021).
[33] J. Polo, V. Ahufinger, F. W. J. Hekking, and A. Minguzzi, Phys. Rev. Lett. **121**, 090404 (2018).
[34] G. Del Pace, K. Xhani, A. Muzi Falconi, M. Fedrizzi, N. Grani, D. Hernandez Rajkov, M. Inguscio, F. Scazza, W. J. Kwon, and G. Roati, Phys. Rev. X **12**, 041037 (2022).
[35] Y. Cai, D. G. Allman, P. Sabharwal, and K. C. Wright, Phys. Rev. Lett. **128**, 150401 (2022).
[36] J. W. Park, B. Ko, and Y. Shin, Phys. Rev. Lett. **121**, 225301 (2018).
[37] S. Eckel, J. G. Lee, F. Jendrzejewski, N. Murray, C. W. Clark, C. J. Lobb, W. D. Phillips, M. Edwards, and G. K. Campbell, Nature **506**, 200 (2014).
[38] P. Kumar, T. Biswas, K. Feliz, R. Kanamoto, M.-S. Chang, A. K. Jha, and M. Bhattacharya, Phys. Rev. Lett. **127**, 113601 (2021).
[39] I. Lesanovsky and W. von Klitzing, Phys. Rev. Lett. **99**, 083001 (2007).
[40] B. E. Sherlock, M. Gildemeister, E. Owen, E. Nugent, and C. J. Foot, Phys. Rev. A **83**, 043408 (2011).
[41] Y. Guo, R. Dubessy, M. d. G. de Herve, A. Kumar, T. Badr, A. Perrin, L. Longchambon, and H. Perrin, Phys. Rev. Lett. **124**, 025301 (2020).
[42] O. Morizot, Y. Colombe, V. Lorent, H. Perrin, and B. M. Garraway, Phys. Rev. A **74**, 023617 (2006).
[43] L. Corman, L. Chomaz, T. Bienaimé, R. Desbuquois, C. Weitenberg, S. Nascimbène, J. Dalibard, and J. Beugnon, Phys. Rev. Lett. **113**, 135302 (2014).
[44] K. C. Wright, R. B. Blakestad, C. J. Lobb, W. D. Phillips, and G. K. Campbell, Phys. Rev. A **88**, 063633 (2013).
[45] D. Naidoo, K. Aït-Ameur, M. Brunel, and A. Forbes, Applied Physics B **106**, 683 (2012).
[46] B. Padhi and S. Ghosh, Phys. Rev. Lett. **111**, 043603 (2013).
[47] J. Polo, R. Dubessy, P. Pedri, H. Perrin, and A. Minguzzi, Phys. Rev. Lett. **123**, 195301 (2019).
[48] R. Benguria and M. Kac, Phys. Rev. Lett. **46**, 1 (1981).
[49] M. B. Plenio, Phys. Rev. Lett. **95**, 090503 (2005).
[50] G. Adesso and F. Illuminati, Journal of Physics A: Mathematical and Theoretical **40**, 7821 (2007).
[51] J. Li, S.-Y. Zhu, and G. Agarwal, Physical Review Letters **121** (2018).
[52] G. Adesso, A. Serafini, and F. Illuminati, Phys. Rev. A **70**, 022318 (2004).
[53] Z.-Y. Fan, H. Qian, X. Zuo, and J. Li, Phys. Rev. A **108**, 023501 (2023).
[54] Z.-Y. Fan, L. Qiu, S. Gröblacher, and J. Li, Laser & Photonics Reviews **17**, 2200866 (2023).
[55] S. Das, P. Kumar, M. Bhattacharya, and T. N. Dey, Phys. Rev. A **110**, 043512 (2024).
[56] X. Zhang, C. ling Zou, L. Jiang, and H. X. Tang, Science Advances **2** (2016).